

Chapter 11

RuBisCO-Inspired Biomimetic Approaches to Reversible CO₂ Capture from Air

Metal Dependence of the H₂O/CO₂ Replacement Penalty

Rainer Glaser*

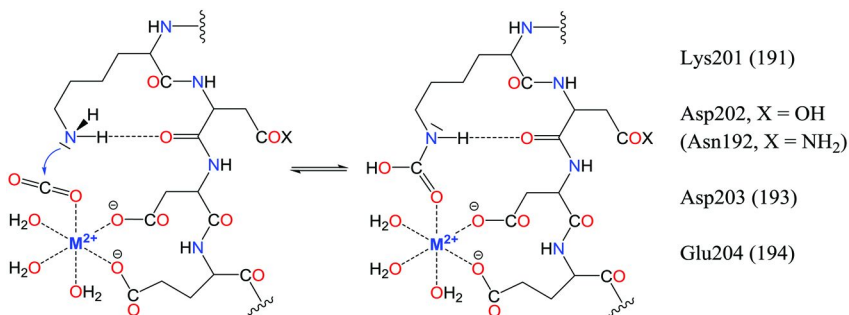
Department of Chemistry, University of Missouri,
Columbia, Missouri 65211, and
Institute of Chemistry, Chinese Academy of Sciences,
Beijing 100190, China
*E-mail: glaserr@missouri.edu

The highly endergonic exchange of a Mg²⁺-coordinated H₂O by CO₂ is an essential feature of rubisco thermochemistry because this H₂O/CO₂ replacement penalty ensures the overall reversibility of the CO₂ capture reaction. While the active site of rubisco employs Mg²⁺ catalysis, rubisco-inspired biomimetic approaches to CO₂ capture from air may involve alternatives to Mg²⁺. To guide the search for alternatives, we studied the metal dependence of the H₂O/CO₂ exchange reaction $\text{CO}_2 + \text{H}_2\text{O}\cdot\text{ML}_2 \rightleftharpoons \text{OCO}\cdot\text{ML}_2 + \text{H}_2\text{O}$ for $\text{M}^{2+} = \text{Mg}^{2+}, \text{Ca}^{2+}, \text{Zn}^{2+}$ (closed-shell, class 1) and $\text{M}^{2+} = \text{Cu}^{2+}, \text{Ni}^{2+}, \text{Co}^{2+}, \text{and Fe}^{2+}$ (open-shell, class 2) at the MP2(full)/6-31G* level. The results suggest that Ca²⁺, Zn²⁺, Cu²⁺, and Co²⁺ are excellent candidates as magnesium alternatives.

Introduction

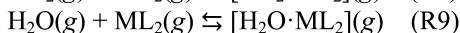
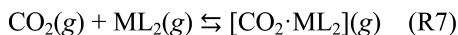
CO₂ scrubbing involves the capture of CO₂ from air by a substrate, the release of CO₂ from the substrate and its collection, and the long-term CO₂ sequestration. Global Research Technologies (GRT) first demonstrated CO₂ capture from air with the ACCESS™ system in 2007 (1), CO₂ capture from the air is the pertinent tool to address CO₂ emissions from distributed sources (2, 3), and, most importantly, CO₂ capture from the air is the method of last resort to combat excessive atmospheric CO₂ concentrations (4, 5). CO₂ scrubbing relies on chemical systems for reversible CO₂ capture and usually involve carbamic acid formation; i.e., CO₂ reaction with amines (6–8), polyamine-based solid adsorbents (9), alkylamine-appended metalorganic framework (10–12), or diamine-appended metal-organic frameworks (13). Alternatives to amine-based capture systems also have been explored and these include, for example, polyethylene glycol promoted CO₂ chemistry (14). The success of any CO₂ capture system relies on the thermochemistry and the kinetics of the CO₂ capture reaction. The thermochemistry of the CO₂ capture reaction must ensure the effective capture as well as the possibility for the subsequent CO₂ release. The kinetics of the CO₂ capture reaction must be such that both the capture and the release of CO₂ are not hindered too much by their activation barriers. Biomimetic CO₂ capture systems are of special interest because they hold promise to meet both the thermodynamic and the kinetic requirements for reversible CO₂ capture. For example, bio-CO₂ capture in carbonic anhydrase II from *Chlorella vulgaris* has been characterized (15). It is our goal to develop rubisco-based biomimetic systems for reversible CO₂ capture from air and the general strategy has been described (16). Our designs of the chemical CO₂ capture and release systems (CCR) are informed by the understanding of the binding of the activator CO₂ (¹³CO₂) in rubisco.

Rubisco (ribulose 1,5-bisphosphate carboxylase/oxygenase, RuBisCO) catalyzes the addition of CO₂ and water to RuBP (d-ribulose 1,5-bisphosphate) in the photosynthetic carbon assimilation via the Calvin-Bassham-Benson cycle and results in two molecules of 3-PGA (3-phospho-d-glycerate) and 0.5 O₂ (17–19). The carboxylation reaction competes with photorespiration, that is, the fixing of molecular O₂ by its addition to RuBP to form one equivalent of 3-PGA and one equivalent of phosphoglycolate. Nearly all carbohydrate production in the biosphere depends on rubisco catalysis and rubisco is the most abundant protein on Earth. Many photosynthetic organisms contain form I rubisco (20) which is comprised of eight large (L) and eight small (S) subunits and the crystal structure of *Spinacia oleracea* (21, 22) provided an early example of a hexa-decameric rubisco (23). Form II rubisco lacks small subunits, generally occurs as L₂, and is exemplified by the bacterial rubisco of *Rhodospirillum rubrum* (24). We focus on form I rubisco and this form also occurs in algae including the green algae *Chlamydomonas reinhardtii* (25) and the red algae *Galdieria sulphuraria* (26).



Scheme 1. Activation of RuBisCO by N-carbamic acid formation with ¹⁴CO₂. Residue numbers refer to the structures of activated RuBisCO in Spinacia oleracea (21, 22) and Rhodospirillum rubrum (24), data in parentheses).

Hartmann and Harpel (27) and Lorimer et al. (28) discussed the mechanism of rubisco catalysis. To exhibit both the carboxylase and oxygenase activities, rubisco must be activated by carbamylation of active-site lysine (Lys) with an activator CO₂ (¹⁴CO₂). The carbamate formed is stabilized both by complexation to Mg²⁺ and by NH···O hydrogen-bonding (Scheme 1). Rubisco activase (29) causes the release of RuBP from unactivated rubisco so that the carbamylation of the lysine by ¹⁴CO₂ can occur. Theoretical studies of the carboxylation and oxygenation reactions of a model system (CH₃COCH₂OH in place of RuBP; Mg²⁺ coordinated by two formate anions as models for Asp203 and Glu204; H₂N-CO₂ as carbamate model of Lys201) have been reported (30, 31).



In the context of our studies of heterocumulenes (32–34) and of nucleophilic additions to heterocumulenes (35–37), we recently analyzed the thermochemistry of a rubisco-based small molecule model of the formation of *N*-methylcarbamic acid (NMCA) by addition of methylamine (CH₃NH₂) to CO₂ considering substrate and product stabilization by an active-side carbonyl model and complexation by a model metal complex ML₂ (16). The model system is described by 14 reactions, the reactions R1 - R14 will be reviewed below, and the thermochemistry was determined at the B3LYP/6-31G* level for the natural case of magnesium M²⁺ = Mg²⁺. Importantly, the complexation of CO₂ to the metal cation M²⁺ requires the replacement a water molecule and our analysis showed that this H₂O/CO₂ replacement is an essential feature of rubisco thermochemistry. The exchange of a ligand water by a CO₂ molecule (reaction R10) is highly endergonic with ΔG₂₉₈(R10) = 15.7 kcal/mol (16, 38), and this H₂O/CO₂ replacement penalty is required to lower the overall exergonicity of the CO₂ capture reaction and to allow overall reversibility. While rubisco employs Mg²⁺ catalysis, one may consider other metals in rubisco-inspired biomimetic approaches to CO₂ capture. As a first step in that direction, we studied the metal dependence of the H₂O/CO₂ replacement penalty for the metal cations M²⁺ = Mg²⁺, Ca²⁺, Zn²⁺, Cu²⁺, Ni²⁺,

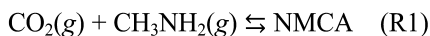
Co²⁺, and Fe²⁺. Here we report on the geometries of the metal formates ML₂ and their electronic structures, on the conformations of the H₂O·ML₂ and OCO·ML₂ adducts, and on the thermochemistry of reactions R7, R9 and R10.

The present study employs second-order Møller-Plesset perturbation theory (MP2) at the MP2(full)/6-31G* level while the earlier work employed density functional theory (DFT) at the B3LYP/6-31G* level (16). Technical aspects of the MP2 computations and especially of the 6-31G* basis sets for the metals will be described below, and here we want to briefly address the major conceptual difference between the approaches. In Hartree-Fock self-consistent field (HF-SCF) theory, each orbital is optimized considering the average electron density of all the other electrons until the iterative process reaches self-consistency. Post-HF electronic structure theory deals with the fact that electrons actually move in ways to avoid each other as much as possible to minimize electron-electron repulsion, that is, the motion of each electron is correlated with the motions of all the other electrons (rather than each electron moving in the field of the average electron density of the other electrons). In post-HF theories, it is common to distinguish between dynamical and non-dynamical (or static) electron correlations. The dynamical correlations of the electrons' motions minimize electron-electron repulsion and especially improve the motions (i.e., the orbitals) of opposite spin electrons. Static correlations become important when only a small gap separates low-lying excited states from the electronic ground state. In such cases one electron configuration may not suffice to describe the wave function. The common DFT approach accounts only for short-range dynamical correlations and neglects static correlations. However, dispersion interactions require long-range dynamical correlations and van der Waals interactions (a.k.a., London interactions or dispersion interactions) are known to affect the accuracy of the reaction thermochemistry of larger systems. To capture dispersion interactions one can perform DFT calculations with empirical London dispersion corrections ((39), DFT-D methods) or one may employ correlation interaction (CI) methods. The CI methods are advantageous because they do not only account for dispersion but also for static electron correlations. Møller-Plesset perturbation theory (MPPT) is a powerful approximation to CI theory and methods development has especially focused on second-order Møller-Plesset perturbation theory (MP2, (40)). With a view to the incorporation of dispersion interactions, one may employ DFT-D or MP2 methods. We chose to employ the MP2 method in the present study because this method also accounts for non-dynamical correlations and this type of electron correlation becomes important in situations with low-lying empty orbitals (i.e., metal d-orbitals) and weak dative bond formation.

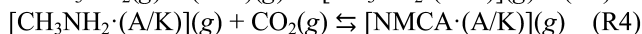
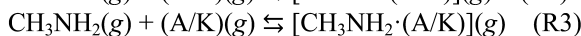
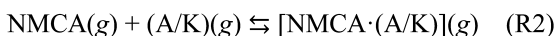
Small Molecule RuBisCO Model

Reaction R1 is the formation of *N*-methylcarbamic acid (NMCA, H₃C—NH—CO—OH) by addition of methylamine to CO₂ in the gas phase (*g*). Three effects of the environment need to be considered in the active site of rubisco (Scheme 1) and these are (A) the stabilization of the product by hydrogen-bonding between NMCA and a model carbonyl compound, (B) the complexation of

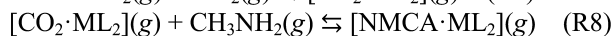
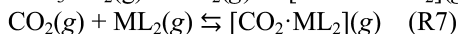
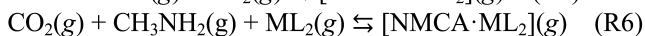
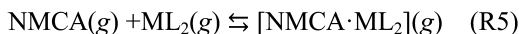
NMCA by a model metal complex ML_2 , and (C) the forced replacement of ligand water by CO_2 at the metal center. We describe the thermochemistry of small molecule model systems $\{CO_2, RNH_2, (A/K), MgL_2\}$ by a system of 14 reactions, R1 - R14, and the case for magnesium ($M^{2+} = Mg^{2+}$) has been analyzed (16).



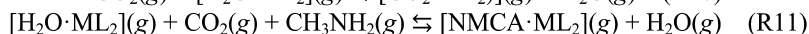
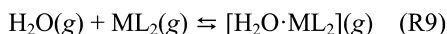
Reaction R2 describes the association of NMCA with a model carbonyl compound (aldehyde A or ketone K) to the aggregate $NMCA \cdot (A/K)$. The presence of the carbonyl compound also may stabilize the amine substrate prior to the addition reaction in the aggregate $CH_3NH_2 \cdot (A/K)$ as described by reaction R3. The combined effects of substrate and product stabilization by the carbonyl compound are reflected in reaction R4, the addition of CO_2 to a carbonyl-aggregated methylamine to form carbonyl-aggregated NMCA. The thermo-chemistry of reaction R4 is a function of reactions R1 - R3: $R4 = R1 + R2 - R3$.



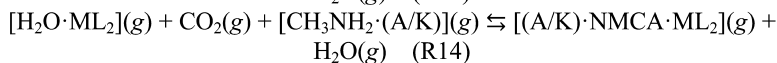
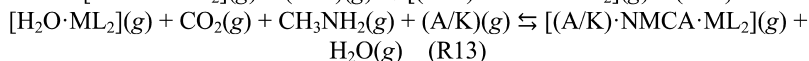
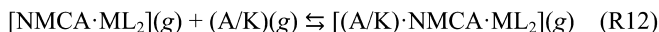
The model metal complex is neutral ML_2 where L is a singly charged anion, and here we use metal(II) formate ($L = HCO_2^-$). Reaction R5 describes the association of NMCA with the formate ML_2 to form the complex $NMCA \cdot MgL_2$. The metal formate will not only stabilize the addition product NMCA, but it also has the potential to stabilize the CO_2 substrate prior to its addition reaction. Reaction R7 describes the association of the CO_2 with MgL_2 to form the pre-reaction substrate aggregate $OCO \cdot ML_2$. The combined effects of CO_2 substrate stabilization and of NMCA product stabilization by the model metal complex are reflected in reaction R8, the addition of methylamine to an M^{2+} -complexed CO_2 molecule to form the M^{2+} -complexed NMCA. The thermochemistry of reaction R8 depends on reactions R1, R5, and R7: $R8 = R1 + R5 - R7$ and with $R6 = R1 + R5$ one obtains $R8 = R6 - R7$.



Prior to the addition reaction, the substrates methylamine and CO_2 and their future binding sites, the model carbonyl compound and the model metal complex, all will be interacting with their respective environments as best as possible. We have shown that the interactions of one water molecule with CH_3NH_2 , a carbonyl, or CO_2 all are relatively weak whereas the complexation of ML_2 by water (reaction R9) stands out dramatically for $M^{2+} = Mg^{2+}$ (16).



The association of one water molecule with magnesium formate, reaction R9, is highly exothermic ($\Delta H_{298}(R9) = -20.7$ kcal/mol) and the reaction also is significantly exergonic ($\Delta G_{298}(R9) = -12.0$ kcal/mol) at the B3LYP/6-31G* level (16). On the other hand, CO₂ binding is weak and, hence, the exchange of a ligand water by a CO₂ molecule, reaction R10 (R10 = R7 - R9) is significantly endothermic with $\Delta H_{298}(R10) = 16.4$ kcal/mol and endergonic with $\Delta G_{298}(R10) = 15.7$ kcal/mol (38) at the B3LYP/6-31G* level (16). Therefore, a reasonable model of the M²⁺-catalyzed NMCA formation must consider the forced replacement of ligand water by CO₂. Accounting for reaction R10 converts reaction R8 to reaction R11: R11 = R8 + R10.



The combined effects of the product stabilization by effects (A) - (C) can now be considered. The model systems (A/K)·NMCA·ML₂ is constructed by addition a carbonyl (aldehyde or ketone) to the appropriate metal formate complexes NMCA·ML₂ (reaction R12). Combination of R11 and R12 results in reaction R13 (R13 = R11 + R12), and considering the aggregation between the substrate methylamine and the carbonyl model (reaction R3) one obtains reaction R14; R14 = R13 - R3 = R11 + R12 - R3. Reaction R14 models the capture of CO₂ and the addition of the M²⁺-complexed CO₂ to a pre-positioned, carbonyl-aggregated methylamine CH₃NH₂·(A/K) to form the M²⁺-complexed and carbonyl-aggregated NMCA, (A/K)·NMCA·ML₂.

Computational Methods

Theoretical Level and Potential Energy Surface Analysis.

Computations were performed at the MP2(full)/6-31G* level of ab initio quantum theory, that is, second-order Møller-Plesset perturbation theory (41–43) was employed with the inclusion of all electrons in the active space. Structures were optimized completely using redundant internal coordinates (44) and vibrational frequencies were computed analytically for stationary structures to determine the thermochemical properties.

Solvation influences the electronic energy of molecular systems because of the mutual polarizations between solute and solvent and solvation also manifests itself in the molecular thermochemistry. One can consider solvation effects in several ways and these include the explicit inclusion of solvent molecules in the model system, the application of continuum solvation models (45), or a combination of both approaches (46). Within each approach one may select various levels of sophistication beginning with the computation of solvation corrections to the energies of gas-phase structures, via the optimization of structures within the solvation model, and on to the determination of optimized structures and their thermochemical properties with the solvation model. In the

present study, we consider the two most important solvent effects. First, we are studying the metal dependence of the H₂O/CO₂ replacement penalty with explicit consideration of the water molecule which is replaced by CO₂ as ligand of the ML₂ complex. Second, we are accounting for the fact that translational entropies in solution are much smaller than the value computed for free or solvated molecules in the gas phase (*vide infra*). This approach will provide meaningful results about the metal dependence of the H₂O/CO₂ replacement penalty and further refinements may include additional corrections for bulk solvation.

Basis Sets

In Pople's nomenclature, the 6-31G* basis set describes the atomic orbitals (AOs) of H, C, and O in the usual fashion (47). Hydrogen atoms are described by a "31G" basis set, that is, by two s-type basis functions which are comprised of 3 or 1 primitive Gaussian functions, respectively. The so-called first-row atoms C and O are described by the 6-31G* basis set, that is, the core 1s AO is described by one basis function comprised of 6 primitive Gaussian functions ("6G" part for the core), and each of the 2s and 2p valence AOs is described by two basis functions comprised of 3 and 1 primitive Gaussian functions, respectively. The Pople basis sets are particularly efficient because s- and p-basis functions in the same sp-shell use primitives with the same exponents. The star in the notation indicates that one set of d-type polarization functions was added to the basis sets of C and O atoms. These polarization functions allow the p-orbitals to deviate from perfect rotational symmetry to better account for polarization in the molecule.

The 6-31G* basis set for magnesium (48) really is a 66-31G* basis set: the 1s core-AO is described by one s-type basis function, and each one of the 2s and 2p core-AOs, respectively, is described by one s- or p-type basis function, respectively, and all of them are comprised of 6 primitive Gaussian functions. The electrons in the valence shell of magnesium (3s, 3p) are described with a split sp-shell and a set of d-functions is added to allow for polarization (0.175).

In analogy, the 6-31G* basis set for calcium (48) really is a 666-31G* basis set: Three core shells (s, sp, sp), a split-valence 31G description of the 4s and 4p atomic orbitals, and one set of d-type polarization functions (0.216).

The 6-31G* basis sets for the transition metals (48) build on the 666-31G basis set of calcium: Three core shells (s, sp, sp; 6G) and a split-valence 31G description of the 4s and 4p AOs. However, the 3d orbitals now are part of the valence shell and they are described by a 31G basis set, that is, with two sets of d-type basis functions. These d-type basis functions also help to polarize the 4s and 4p orbitals. In addition, one set of f-type polarization functions is added to allow for more flexibility of the d-orbitals (f-exponents, Zn – Fe: 0.8).

The calculations employed sets of 6 Cartesian d-type orbitals (6D) which were later combined to sets of 5 spherical d-orbitals and one additional s-type basis function. Sets of seven pure f-functions were used throughout (7F).

Molecular Entropies

While molecular entropies for vibrational and rotational motions in solution can be approximated well by gas phase computations (49), the translational entropy is greatly reduced in solution relative to the value computed for the free molecules in the gas phase (50–52). Wertz (53) derived an equation that relates the entropy of solvation ΔS_{sol} to the gas-phase entropy S_{gas} at 25 °C and 1 atm via $\Delta S_{\text{sol}} = -0.46 \cdot (\Delta S_{\text{gas}} - 14.3)$. We employ the Wertz equation to compute the translational molecular entropy in solution via $S_{\text{tr,W}} = S_{\text{tr,gas}} + S_{\text{tr,sol}} = 0.54 \cdot S_{\text{tr}} + 6.578$, and we then use the corrected molecular entropy $S_{\text{W}} = S_{\text{vib,gas}} + S_{\text{rot,gas}} + S_{\text{tr,W}} = S_{\text{gas}} + S_{\text{tr,sol}}$ instead of the directly computed molecular entropy S to compute free enthalpies.

Total Energies and Thermochemistry

The most pertinent results of the potential energy surface analysis at the MP2(full)/6-31G* level are summarized in Table 1 and the data include total energies $E(\text{MP2}(\text{full})/6-31\text{G}^*)$, vibrational zero-point energies (ZPE) and thermal energies (TE), and molecular entropies (S). The molecular entropy includes contributions from vibrational, rotational and translational motions, $S = S_{\text{vib}} + S_{\text{rot}} + S_{\text{tr}}$. The computed molecular translational entropy (S_{tr}) also is listed together with a corrected total molecular entropy (S_{W}) which accounts for the reduced translational entropy in solution.

Table 1. Total Energies and Thermochemical Data

<i>Molecule</i>	<i>E(MP2)^a</i>	<i>ZPE^b</i>	<i>TE^c</i>	<i>S^d</i>	<i>S_{tr}^e</i>	<i>S_W^f</i>
H ₂ O	-76.19924	13.5	15.3	45.1	34.6	35.8
CO ₂	-188.11836	7.3	8.9	51.2	37.3	40.6
<i>Diformate, ML₂</i>						
Mg ²⁺ , tetra	-577.15278	30.8	35.5	86.5	40.1	74.7
Ca ²⁺ , tetra	-1054.28288	29.9	35.0	92.5	40.5	80.4
Zn ²⁺ , tetra	-2155.28461	30.7	35.4	87.5	41.0	75.2
Cu ²⁺ , square	-2016.45207	30.9	35.5	87.5	41.0	75.2
Ni ²⁺ , square	-1884.35764	31.7	35.9	81.9	40.9	69.7
Co ²⁺ , square	-1758.90937	31.7	35.9	83.4	40.9	71.1
Fe ²⁺ , square	-1639.88556	30.8	35.5	86.8	40.9	74.6
<i>Hydrate, L₂M·OH₂</i>						
Mg ²⁺ , tppy-HB2ax	-653.39401	46.3	52.9	101.5	40.6	89.5
Ca ²⁺ , tppy-HB1ax	-1130.52277	45.4	52.4	107.3	40.9	95.1
Zn ²⁺ , tppy-HB2ax	-2231.52231	46.3	52.9	101.8	41.3	89.3

Continued on next page.

Table 1. (Continued). Total Energies and Thermochemical Data

<i>Molecule</i>	<i>E</i> (MP2) ^a	<i>ZPE</i> ^b	<i>TE</i> ^c	<i>S</i> ^d	<i>S_{tr}</i> ^e	<i>S_w</i> ^f
Cu ²⁺ , spy-HB2a	-2092.68542	46.6	53.0	101.3	41.3	88.8
Ni ²⁺ , spy-HB2a	-1960.57769	47.0	53.2	96.9	41.2	84.5
Co ²⁺ , spy-HB2a	-1835.14561	47.1	53.3	97.8	41.6	85.4
Fe ²⁺ , spy-HB2a	-1716.16992	47.7	53.6	93.7	41.2	81.3
Cu ²⁺ , spy-HB2b	-2092.68428	46.1	52.8	104.6	41.3	92.1
Ni ²⁺ , spy-HB2b	-1960.57747	46.4	53.0	102.7	41.2	90.3
Co ²⁺ , spy-HB2b	-1835.14594	46.9	53.8	98.7	41.6	86.3
Fe ²⁺ , spy-HB2b	-1716.17001	47.6	53.5	94.6	41.2	82.2
<i>CO₂-Agg, L₂M·OCO</i>						
Mg ²⁺ , tpy-INA1ax	-765.28614	38.7	45.9	110.0	41.1	97.7
Ca ²⁺ , tpy-INA1ax	-1242.41900	37.8	45.4	116.8	41.4	104.3
Zn ²⁺ , tpy-INA1ax	-2343.41681	38.5	45.8	112.6	41.8	99.9
Cu ²⁺ , spy-INA2	-2204.58715	38.8	45.9	112.7	41.7	100.1
Ni ²⁺ , spy-INA2	-2072.48821	39.5	46.3	107.1	41.7	94.6
Co ²⁺ , spy-INA1	-1947.04467	39.1	46.0	110.4	41.7	97.9
Fe ²⁺ , spy-INA2, s	-1828.06284	39.6	46.2	103.8	41.6	91.2
Fe ²⁺ , spy-INA2, l	-1828.03511	39.4	46.3	109.4	41.6	96.9

^a Total energy E(MP2(full)/6-31G*), in atomic units. ^b Vibrational zero-point energy (ZPE) in kcal/mol. ^c Thermal energy (TE) in kcal/mol. ^d Molecular entropy (*S*) in cal/(K·mol). ^e Molecular translational entropy (*S_{tr}*) in cal/(K·mol) as computed. ^f Total molecular entropy (*S_w*) in cal/(K·mol) based on reduced translational entropy.

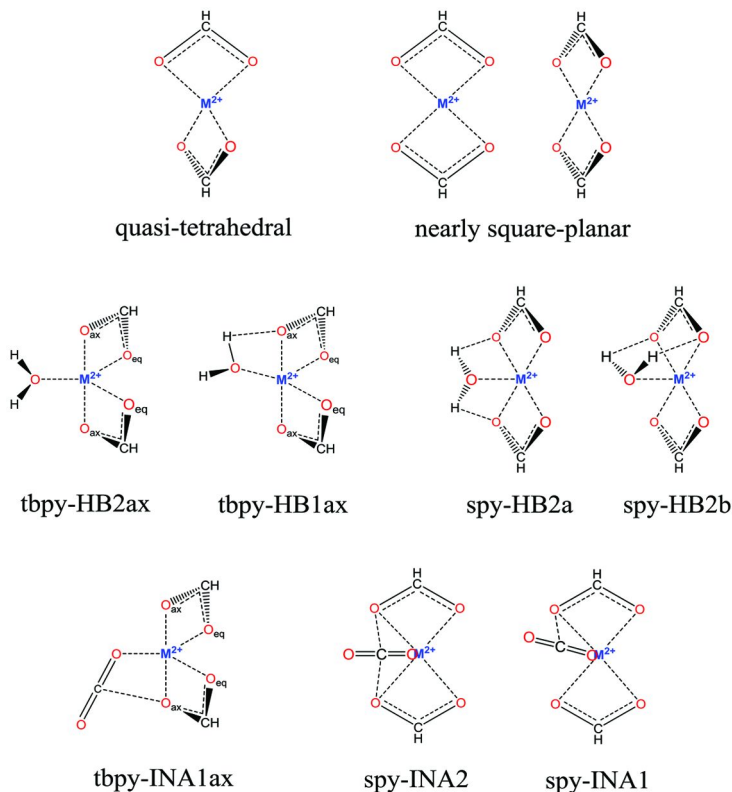
Computations were performed with Gaussian09 (54) on various platforms including the *Lewis* cluster system of the University of Missouri Bioinformatics Consortium (55).

Molecular Structures

The structures naturally fall into two classes (Scheme 2). The formates of magnesium, calcium, and zinc feature quasi-tetrahedral coordination (qt) of the metal ion (closed-shell systems), and they are clearly distinct from the (nearly) square planar (spl) coordination modes of the formates of copper, nickel, cobalt and iron (unfilled d-shells). The H₂O and CO₂ adducts of the formates ML₂ reflect the structural distinctions of the formates and also fall into two classes.

The optimized structures of the formates ML₂ of M = Mg, Ca, and Zn are shown in the left column of Figure 1, and the structures of the formates of M = Cu, Ni, Co and Fe are shown in Figure 2. The structures of their D·ML₂ complexes of the closed-shell systems are included in Figure 1 and the others are shown in

Figures 3 - 5. Major structural parameters are given in the captions of Figures 1 and 2 for the formates, in Table 2 for the hydrates, and in Table 3 for the CO₂ complexes. Complete Cartesian coordinates of all stationary structures can be obtained via email from the author.



Scheme 2. Geometries of the formates ML_2 (top) and of their complexes $H_2O \cdot ML_2$ (center) and $OCO \cdot ML_2$ (bottom). The formates of the closed-shell systems with $M = Mg, Ca,$ and Zn (class 1) feature quasi-tetrahedral structures (qt) while the formates of the open-shell systems with $M = Cu, Ni, Co,$ and Fe (class 2) feature square-pyramidal structures (spy). The $D \cdot ML_2$ complexes of the closed-shell systems adopt trigonal-bipyramidal structures (tbpy) while the complexes of the open-shell systems prefer square-pyramidal structures (spy). Conformational aspects are discussed in the text.

The distances $d(M \cdots O)$ between M^{2+} and a ligand O atom in the formates ML_2 (Figures 1 and 2) roughly parallel M^{2+} ion sizes (56); $M^{2+} = Mg^{2+}$ (86 pm), Ca^{2+} (114 pm), Zn^{2+} (88 pm), Cu^{2+} (87 pm), Ni^{2+} (83 pm), Co^{2+} (79 pm), and Fe^{2+} (75 pm). The Ca^{2+} ion is much larger than Mg^{2+} , Zn^{2+} ion is the best match for Mg^{2+} , and the ions in class 2 allow for a systematic decrease in M^{2+} size.

The additional coordination of one donor ligand D to a tetrahedral formate results in trigonal bipyramidal structures (tbpy) in which one formate O-atom of each ligand occupies an axial position (O_{ax}) while the second O-atom of each formate occupies an equatorial position (O_{eq}). The additional ligand D occupies an equatorial position. The addition of donor ligand D to a (nearly) square-planar formate results in (nearly) square-pyramidal structures (spy) in which the additional ligand occupies the unique axial position. These main structural motives are further distinguished depending on the orientation of the ligand D.

Table 2. Major Structural Parameters of Hydrates $H_2O \cdot ML_2^{a-d}$

<i>Mol.</i>	$d(M \cdots O)$	$\mathcal{D}(OCO)$	$d(M \cdots D)$	<i>Other</i>
MgL ₂	2.098 & 2.063	122.2	2.064	$\mathcal{D}(O_{ax}\text{-M-D})$ 89.11 $d(H \cdots O_{ax})$ 2.862
CaL ₂	2.446 & 2.384 2.396 & 2.382	124.3 124.5	2.403	$\mathcal{D}(O_{ax}\text{-M-D})$ 67.53 $d(H \cdots O_{ax})$ 2.065
ZnL ₂	2.113 & 1.999	121.8	2.055	$\mathcal{D}(O_{ax}\text{-M-D})$ 85.63 $d(H \cdots O_{ax})$ 2.699
CuL ₂ HB2a	1.970 & 2.016	120.3	2.182	$\mathcal{D}(O\text{-M-D})$ 84.77 $d(H \cdots O)$ 2.470
CuL ₂ HB2b	1.986 & 2.002 1.984 & 1.972	120.5 120.3	2.169	$\mathcal{D}(O\text{-M-D})$ 91.61 $d(H \cdots O)$ 2.836, 3.159
NiL ₂ HB2a	1.908 & 1.879	118.1	2.396	$\mathcal{D}(O\text{-M-D})$ 80.66 $d(H \cdots O)$ 2.396
NiL ₂ HB2b	1.893 & 1.895 1.884 & 1.885	118.3 118.1	2.325	$\mathcal{D}(O\text{-M-D})$ 94.95 $d(H \cdots O)$ 3.229, 3.045
CoL ₂ HB2a	1.961 & 1.943	119.1	2.149	$\mathcal{D}(O\text{-M-D})$ 86.45 $d(H \cdots O)$ 2.502
CoL ₂ HB2b	1.954 & 1.955 1.939 & 1.941	119.3 119.1	2.133	$\mathcal{D}(O\text{-M-D})$ 92.67 $d(H \cdots O)$ 2.872, 2.855
FeL ₂ HB2a	1.995 & 1.983	119.5	1.971	$\mathcal{D}(O\text{-M-D})$ 87.36 $d(H \cdots O)$ 2.411
FeL ₂ HB2b	1.992 & 1.994 1.974 & 1.976	119.7 119.5	1.969	$\mathcal{D}(O\text{-M-D})$ 91.42 $d(H \cdots O)$ 2.663, 2.672

^a $d(M \cdots O)$ and $\mathcal{D}(OCO)$ values in one row refer to the same formate. ^b Class 1 systems: In each row, the $d(M \cdots O)$ values refer to O_{ax} and O_{eq} , respectively. Data for the formate more engaged in HB are listed first. HB contacts refer to the closer O_{ax} . ^c Class 2, HB2a systems: The first $d(M \cdots O)$ value as well as the $\mathcal{D}(O\text{-M-D})$ and $d(H \cdots O)$ values refer to the formate-O with the HB contact. ^d Class 2, HB2b systems: $d(M \cdots O)$ and $\mathcal{D}(OCO)$ values in the first row refer to the formate more engaged in HB contacts. The $\mathcal{D}(O\text{-M-D})$ value and the first $d(H \cdots O)$ value refer to the formate-O with the best HB contact.

Table 3. Major Structural Parameters of CO₂-Aggregates OCO·ML₂^{a-d}

<i>Mol.</i>	<i>d(M··O)</i>	<i>∠(OCO)</i>	<i>d(M··D)</i>	<i>Other</i>
MgL ₂	2.101 & 2.055 2.068 & 2.048	121.9 121.9	2.210	∠(M-O-C) 124.35 ∠(O-M-O-C) -2.03 <i>d</i> (INA) 2.830
CaL ₂	2.405 & 2.383 2.374 & 2.372	124.2 124.3	2.551	∠(M-O-C) 125.53 ∠(O-M-O-C) 1.08 <i>d</i> (INA) 2.826
ZnL ₂	2.073 & 2.014 2.043 & 2.009	121.1 121.2	2.234	∠(M-O-C) 125.82 ∠(O-M-O-C) 0.36 <i>d</i> (INA) 2.808
CuL ₂	1.975 & 1.963	119.9	2.319	∠(M-O-C) 113.84 ∠(O _f -M-O) 85.86 <i>d</i> (INA) 3.110
NiL ₂	1.880 & 1.875	117.7	2.527	∠(M-O-C) 103.56 ∠(O _f -M-O) 82.91 <i>d</i> (INA) 2.991
CoL ₂	1.966 & 1.961 1.957 & 1.958	119.2 119.2	2.236	∠(M-O-C) 115.11 ∠(O _f -M-O) 86.93 <i>d</i> (INA) 3.010 & 3.238
FeL ₂ short	1.973 & 1.977	119.2	2.027	∠(M-O-C) 114.78 ∠(O _f -M-O) 89.91 <i>d</i> (INA) 3.002
FeL ₂ long	1.911 & 1.909	117.9	2.745	∠(M-O-C) 106.42 ∠(O _f -M-O) 78.16 <i>d</i> (INA) 3.110

^a For all CO₂ aggregates: *d*(M··O) and ∠(OCO) values in one row refer to the same formate. ^b In the absence of C_s-symmetry, data in the first row refer to the formate closer to CO₂. ^c ∠(M-O-C) is the angle between the (M··D) dative bond and OCO. ^d ∠(O_f-M-O) is the angle between CO₂-O and the (M··O) dative bond of the formate-O involved in INA. ^e *d*(INA) is the distance between the CO₂-C and the closest formate-O.

In the hydrate complexes (D = OH₂) of class 1 systems (Figure 1, center column), there exists the possibility for hydrogen bonding between the ligand water and one or two proximate formate O-atoms (Scheme 2). In the H₂O·CaL₂ complex, the ligand water is placed to optimized one H-bond to one axial formate-O (HB1ax) with a short contact of 2.065 Å, while the H₂O·ML₂ complexes with M = Mg, Zn feature two equivalent HB-contacts to the two axial formate-O atoms (HB2ax) which are much longer (> 2.65 Å).

In the carbon dioxide complexes (D = OCO) of class 1 systems (Figure 1, right column), there exists the possibility for incipient nucleophilic attack (INA) interaction (57, 58) between the electrophilic C-atom and one or two proximate formate O-atoms. In the OCO·ML₂ complexes with M = Mg, Ca, Zn, the ligand CO₂ is placed to optimize one INA to one axial formate-O (tbpy-INA1ax) and allows the proximate nucleophilic formate-O to approach the electrophilic CO₂-carbon to a distance of *d*(INA) ≈ 2.80 - 2.83 Å (Table 3).

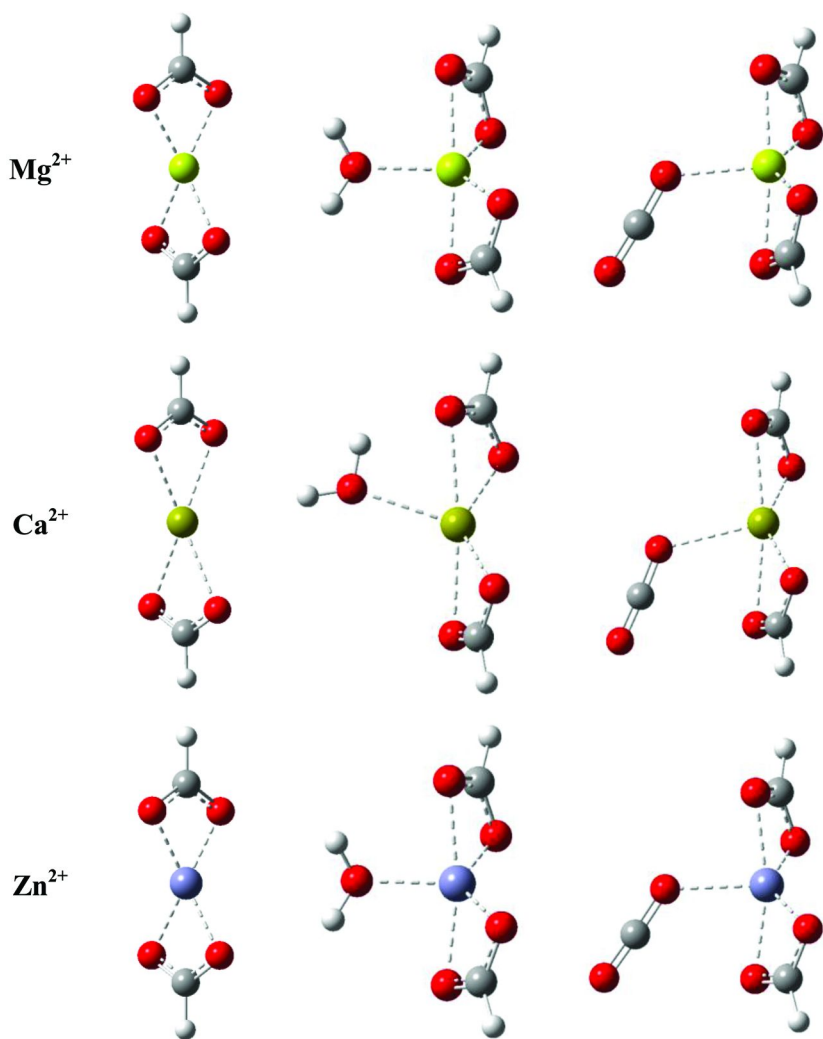


Figure 1. Optimized structures of the metal formates ML_2 (left) and of complexes $D:ML_2$ formed with water (center) and CO_2 (right) with $M^{2+} = Mg^{2+}$, Ca^{2+} , and Zn^{2+} . Structural parameters $d(M\cdots O)$ and $\angle(OCO)$ of formates ML_2 : Mg^{2+} : 2.044 Å, 121.8°; Ca^{2+} : 2.366 Å, 124.2°; and Zn^{2+} : 2.007 Å, 120.9°.

In the hydrate complexes ($D = OH_2$) of the open-shell systems in class 2, the water molecule can be oriented in such a way that water forms one HB contact with each ligand (HB2a) and such structures correspond to minima for every formate of this type (Figure 3). Alternatively, the ligand water can be oriented to engage preferentially with one of the ligand (HB2b) and such structures also correspond to minima for every formate (Figure 4). The HB2b structures allow for a somewhat closer approach of water to the metal center. Irrespective of the specific type of HB

contact, the $d(M\cdots O)$ distances are markedly longer for the class 2 ions than for the closed-shell systems. Note especially that the $d(M\cdots O)$ distance in the $H_2O\cdot NiL_2$ complex is almost as long as that in $H_2O\cdot CaL_2$.

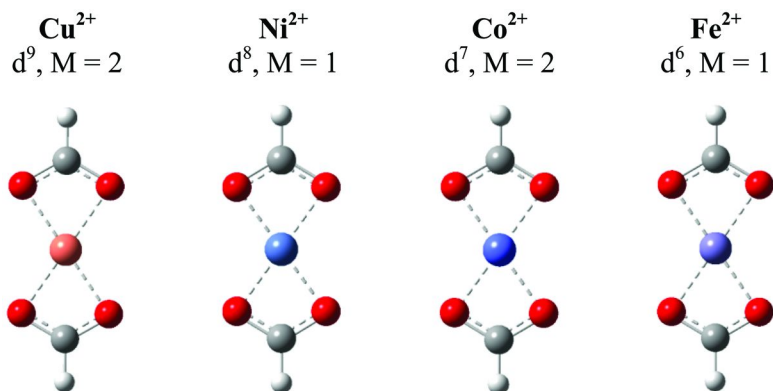


Figure 2. Optimized structures of the metal formates ML_2 of the open-shell systems with $M^{2+} = Cu^{2+}, Ni^{2+}, Co^{2+},$ and Fe^{2+} . Structural parameters $d(M\cdots O)$ and $\angle(OCO)$ of formates ML_2 : Cu^{2+} : 1.959 Å, 119.6°; Ni^{2+} : 1.871 Å, 117.4°; Co^{2+} : 1.895 Å, 117.8°; and Fe^{2+} : 1.943 Å, 118.8°.

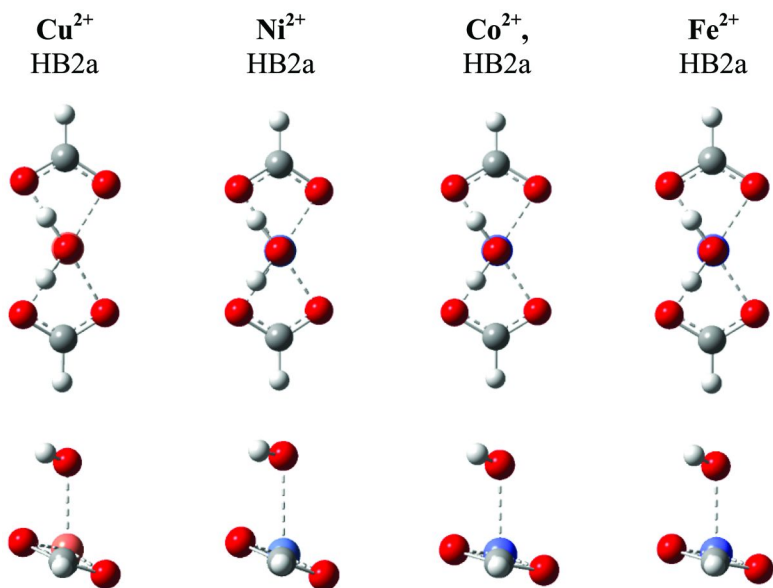


Figure 3. Optimized structures of the hydrate complexes $D\cdot ML_2$ of the open-shell systems with $M^{2+} = Cu^{2+}, Ni^{2+}, Co^{2+},$ and Fe^{2+} . HB2a complexes are viewed down the $H_2O\cdots M$ bonding line (top row) and from the side (second row).

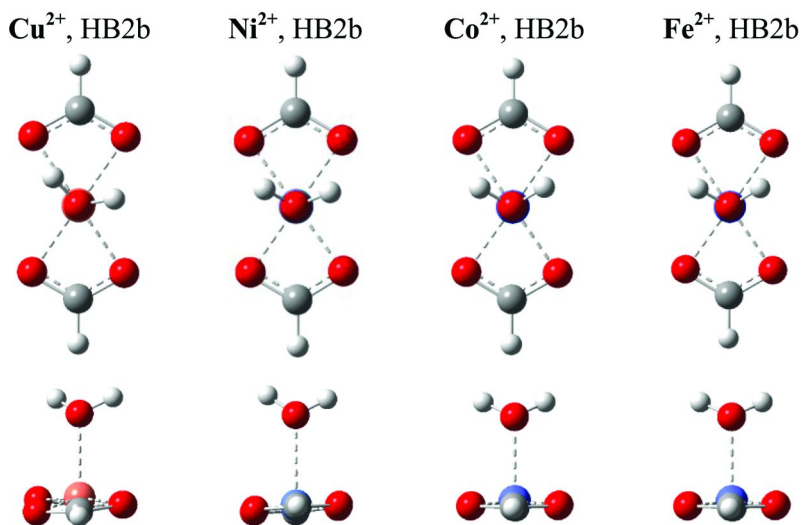


Figure 4. Optimized structures of the hydrate complexes $D \cdot ML_2$ of the open-shell systems with $M^{2+} = Cu^{2+}, Ni^{2+}, Co^{2+},$ and Fe^{2+} . HB2b complexes are viewed down the $H_2O \cdots M$ bonding line (top row) and from the side (second row).

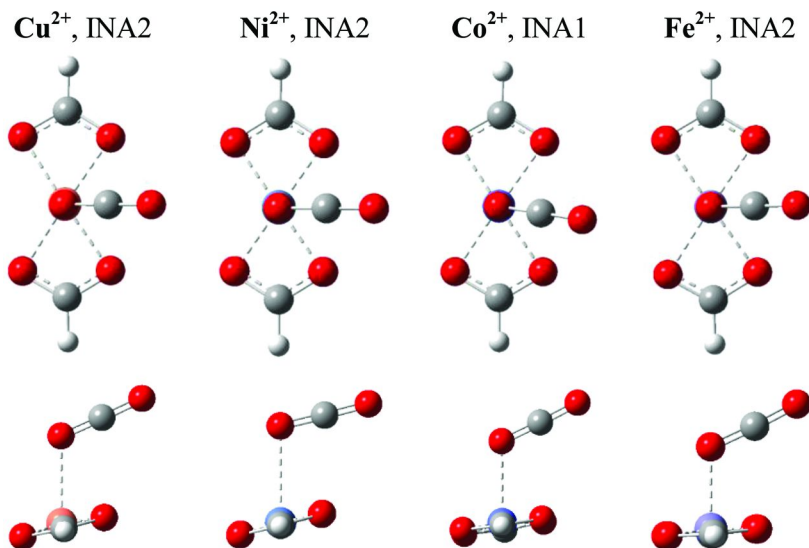


Figure 5. Optimized structures of the CO_2 complexes $D \cdot ML_2$ of the open-shell systems with $M^{2+} = Cu^{2+}, Ni^{2+}, Co^{2+},$ and Fe^{2+} . The complexes are viewed down the $OCO \cdots M$ bonding line (top row) and from the side (second row).

In the class 2 systems, the $\text{OCO}\cdot\text{ML}_2$ complexes (Figure 5) with $M = \text{Cu}, \text{Ni}$, and Fe feature double INA involving one O-atom of each formate (spy-INA2), while the $\text{OCO}\cdot\text{CoL}_2$ complex prefers a structure with one stronger INA contact (spy-INA1). The contacts $d(\text{INA}) \approx 3.0 - 3.1 \text{ \AA}$ are slightly longer than for class 1 ions (Table 4).

The geometries indicate that H_2O is a much better donor compared to CO_2 and this is true for all metal ions. The $d(\text{M}\cdots\text{O})$ distances are about $0.16 \pm 0.02 \text{ \AA}$ shorter for $\text{H}_2\text{O}\cdot\text{ML}_2$ than for $\text{OCO}\cdot\text{ML}_2$ for the class 1 metal ions and the same is true for Cu^{2+} and Ni^{2+} (Tables 3 and 4). However, this difference is reduced to 0.10 \AA and 0.06 \AA for Co^{2+} and Fe^{2+} , respectively.

Binding Energies and $\text{H}_2\text{O}/\text{CO}_2$ Replacement Penalty

Relative and reaction energies computed at the MP2(full)/6-31G* level are summarized in Table 4, and Figures 6 ($\Delta E, \Delta H_{298}$) and 7 ($\Delta G_{298}, \Delta G_W$) illustrate the cost of replacement (in kcal/mol) of water by CO_2 in complexes (R10) and binding energies of ML_2 with water (R9) and CO_2 (R7).

Theoretical Level Dependency

The B3LYP/6-31G* data for Mg^{2+} (16) are included in Table 4 for comparison. The MP2(full)/6-31G* data of the present study indicate stronger binding for water ($\Delta H_{298}(\text{R9}) = -24.1 \text{ kcal/mol}$) and CO_2 ($\Delta H_{298}(\text{R7}) = -7.9 \text{ kcal/mol}$) than at the B3LYP/6-31G* level, but the enthalpy of the exchange reaction ($\Delta H_{298}(\text{R10}) = 16.2 \text{ kcal/mol}$) is just about the same as the value computed at the DFT level. The enthalpy differences at the two levels account for all but 0.24 kcal/mol of the differences between the $\Delta G_{298}(\text{R7})$ and $\Delta G_{298}(\text{R9})$ values computed at the two levels, and it accounts essentially for all of the difference between the $\Delta G_{298}(\text{R10})$ values computed at the DFT (15.7 kcal/mol) and MP2 (15.5 kcal/mol) levels.

Wertz Correction of Molecular Translational Entropy

The comparison of the DFT and MP2 data for the Mg^{2+} systems suggests that both theoretical levels provide rather similar thermochemical parameters, which is encouraging. The thermochemical parameters are computed for the gas phase and we pointed out above that molecular entropies for vibrational and rotational motions in solution can be approximated well by gas phase computations while translational entropies are significantly reduced in solution relative to the free molecules in the gas phase. Hence, we employed the Wertz equation (53) to compute the translational molecular entropy in solution via $S_{\text{tr,W}} = 0.54 \cdot S_{\text{tr}} + 6.578$ and we employed the corrected molecular entropy $S_W = S_{\text{vib,gas}} + S_{\text{rot,gas}} + S_{\text{tr,W}}$ (Table 1) in the computation of the ΔG_W values (Table 4).

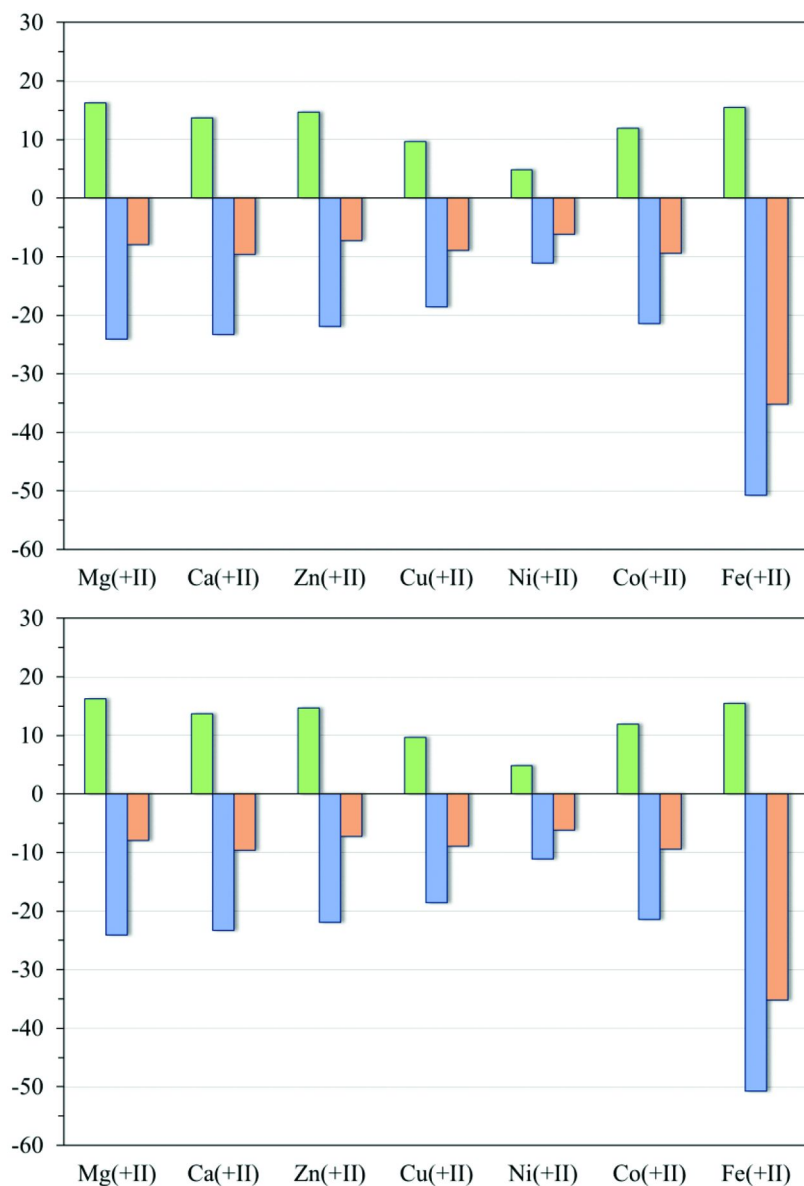


Figure 6. Cost of replacement (in kcal/mol) of water by carbon dioxide in complexes $D \cdot ML_2$ (left column, green online) and binding energies of ML_2 with water (center column, blue online) and CO_2 (right column, red online). Top: ΔE . Bottom: ΔH_{298} .

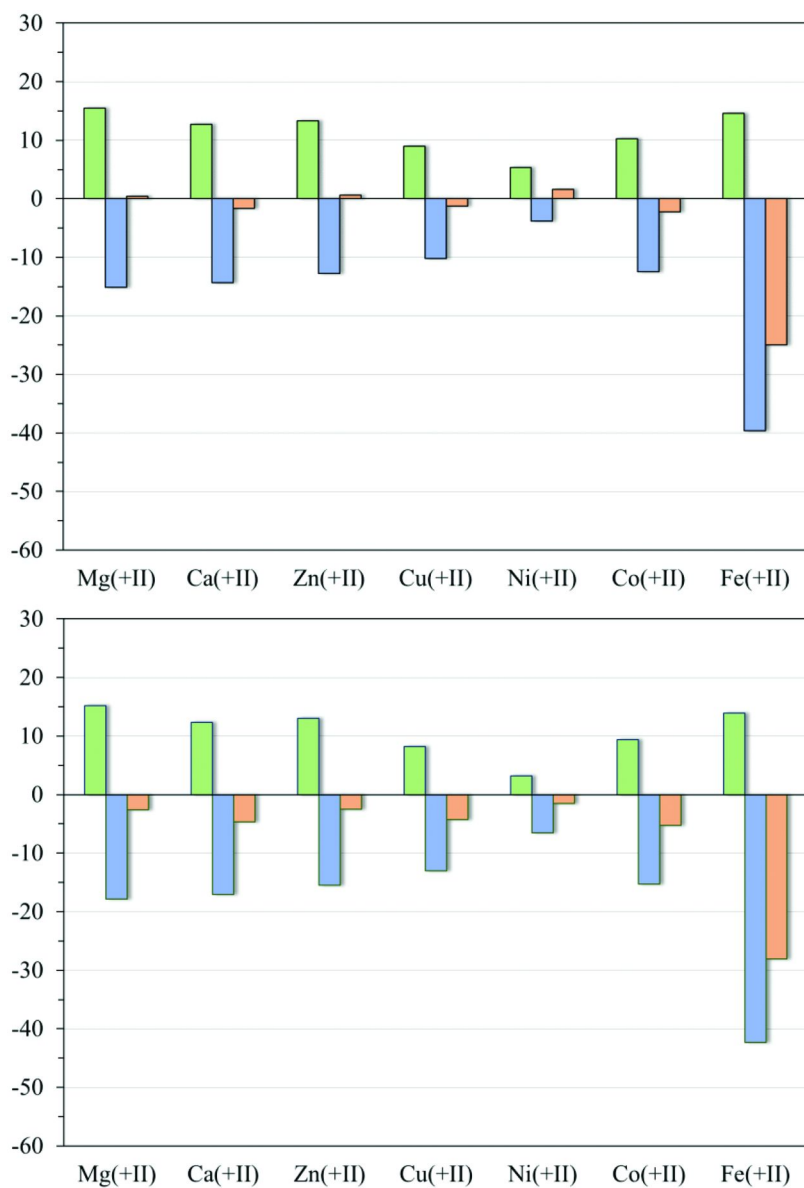


Figure 7. Cost of replacement (in kcal/mol) of water by carbon dioxide in complexes $D \cdot ML_2$ (left column, green online) and binding energies of ML_2 with water (center column, blue online) and CO_2 (right column, red online). Top: ΔG_{298} . Bottom: ΔG_W .

Table 4. Relative and Reaction Energies^a

<i>Parameter</i>	ΔE^b	ΔH_f^c	ΔH^d	ΔG^e	ΔG_{wf}^f
HB2a vs. HB2b					
Cu(+II)	-0.72	-0.29	-0.54	0.45	0.45
Ni(+II)	-0.14	0.44	0.09	1.83	1.83
Co(+II)	0.21	0.38	0.29	0.56	0.56
Fe(+II)	0.06	0.19	0.12	0.40	0.40
R10: L₂M·OH₂ (HB2b) + CO₂ ⇌ L₂M·OCO + H₂O					
Mg(+II) ^g	16.47	15.95	16.42	15.69 ^h	
Mg(+II)	16.93	15.57	16.23	15.52	15.23
Ca(+II)	14.36	12.96	13.70	12.69	12.39
Zn(+II)	15.45	13.93	14.73	13.31	13.00
Cu(+II)	10.20	9.08	9.63	9.02	8.27
Ni(+II)	5.26	4.55	4.90	5.39	3.25
Co(+II)	12.79	11.18	11.97	10.28	9.41
Fe(+II)	16.50	14.75	15.52	14.60	13.89
R7: L₂M + CO₂ ⇌ L₂M·OCO					
Mg(+II) ^g	-6.52	-5.01	-4.33	3.72 ^h	
Mg(+II)	-9.41	-8.72	-7.89	0.39	-2.63
Ca(+II)	-11.15	-10.52	-9.63	-1.61	-4.64
Zn(+II)	-8.68	-8.12	-7.20	0.60	-2.45
Cu(+II)	-10.49	-9.85	-8.96	-1.22	-4.27
Ni(+II)	-7.66	-7.15	-6.18	1.57	-1.48
Co(+II)	-10.63	-10.48	-9.40	-2.22	-5.26
Fe(+II)	-36.97	-35.44	-35.19	-24.99	-28.03
R9: L₂M + H₂O ⇌ L₂M·OH₂ (HB2b)					
Mg(+II) ^g	-22.99	-20.96	-20.74	-11.99	
Mg(+II)	-26.35	-24.30	-24.12	-15.13	-17.86
Ca(+II)	-25.51	-23.48	-23.33	-14.30	-17.03
Zn(+II)	-24.14	-22.05	-21.92	-12.71	-15.45
Cu(+II)	-20.68	-18.93	-18.60	-10.24	-12.98
Ni(+II)	-12.92	-11.69	-11.07	-3.82	-6.56

Continued on next page.

Table 4. (Continued). Relative and Reaction Energies^a

Parameter	ΔE^b	ΔH_f^c	ΔH^d	ΔG^e	ΔG_W^f
Co(+II)	-23.42	-21.66	-21.38	-12.50	-15.23
Fe(+II)	-53.47	-50.19	-50.71	-39.59	-42.32

^a All values in kcal/mol. ^b Relative or reaction energy, ΔE , computed using total energies. ^c Relative or reaction enthalpy at absolute zero Kelvin, $\Delta H_0 = \Delta E + \Delta(\text{ZPE})$. ^d Relative or reaction enthalpy at standard conditions (298.15 Kelvin), $\Delta H = \Delta E + \Delta(\text{TE})$. ^e Relative or reaction free enthalpy at standard conditions (298.15 Kelvin), $\Delta G = \Delta H - T\Delta(S)$. ^f Relative or reaction free enthalpy at standard conditions (298.15 Kelvin) with Wertz correction for translational entropy, $\Delta G_W = \Delta H - T\Delta(S_W)$. ^g B3LYP/6-31G*, ref. (16). ^h $S(\text{CO}_2) = 51.17 \text{ cal}/(\text{mol}\cdot\text{K})$ at B3LYP/6-31G* and was listed erroneously in ref. (16) as $S(\text{CO}_2) = 39.63 \text{ cal}/(\text{mol}\cdot\text{K})$.

If molecular translational entropy is reduced in solution, then any association reaction in solution will suffer less of an entropy penalty compared to the association reaction in the gas phase; $\Delta G_W < \Delta G_{298}$. This is borne out by the ΔG_W values for the formations of the $\text{OCO}\cdot\text{ML}_2$ complexes ($\Delta G_{298} - \Delta G_W \approx 3.04 \text{ kcal/mol}$) and of the $\text{H}_2\text{O}\cdot\text{ML}_2$ complexes ($\Delta G_{298} - \Delta G_W \approx 2.74 \text{ kcal/mol}$). Note in particular that the CO_2 complexes are predicted to be bound in solution: $\Delta G_W(\text{R7}) < 0$ for all of the cases studied (Figure 7).

Conformational Preference Energy of $\text{H}_2\text{O}\cdot\text{ML}_2$ Complexes

We optimized the $\text{H}_2\text{O}\cdot\text{ML}_2$ complexes of the class 2 systems with two conformations about the $\text{H}_2\text{O}\cdot\text{M}$ axis, HB2a and HB2b. On the potential energy surface, the HB2a conformation is preferred for Cu^{2+} and Ni^{2+} while the HB2b conformation is preferred for Co^{2+} and Fe^{2+} . Thermal energies and molecular entropies provide advantages to the HB2b conformation, the free enthalpies ΔG all show a small preference for HB2b, and rotation about the $\text{H}_2\text{O}\cdot\text{M}$ axis is essentially free. Reactions R9 and R10 have been evaluated using the HB2b structures.

Alternatives to Magnesium

The major reason for the exergonicity of the CO_2 capture reaction with rubisco mimics is the coordination of the carbamic acid adduct to the metal cation (R5). The overall exergonicity of the CO_2 capture reaction is moderated by the $\text{H}_2\text{O}/\text{CO}_2$ replacement penalty (R10) which allows for overall reversibility. The most important parameter of the present study clearly is $\Delta G_W(\text{R10})$; it needs to be positive and of significant magnitude. In addition, it is advantageous if the water binding is not too strong; $|\Delta G_W(\text{R9})|$ should be relatively small because the reaction rate constant for the dehydration is inversely proportional to the strength of the water binding.

Among all of the metals studied, magnesium shows the highest $\Delta G_W(\text{R10})$ value. Iron shows the second highest $\text{H}_2\text{O}/\text{CO}_2$ replacement penalty, but the very high water affinity is a disadvantage for iron(II). The data show that the

closed-shell systems calcium and zinc are excellent candidates to serve as potential magnesium alternatives. The data further suggest that the open-shell transition metal ions copper(II) and cobalt(II) might be possible magnesium alternatives.

Reaction Free Enthalpies and Equilibrium Concentrations

We computed reaction free enthalpies ΔG (also referred to as Gibbs free energies) and these values provide the equilibrium constants K_i via the familiar equation $\Delta G_i = -RT \cdot \ln(K_i)$, or equivalently $K_i = \exp(-\Delta G_i/RT)$, where ΔG_i is the free enthalpy of reaction i , R is the gas constant, and T is the absolute temperature. With Chicone, we recently described mathematical methods for the determination of steady-state concentrations of all species in multiequilibria systems using the traditional equilibrium approach or with the dynamical approach (59). The dynamical approach to the equilibrium problem involves the formulation of the kinetic rate equations for each species using general mass action kinetics theory, which together constitute a nonlinear system of ordinary differential equations (ODEs). The equilibrium concentrations are determined by evolving the initial concentrations via this dynamical system to their steady state (59).

Every equilibrium reaction is described by two reaction rate constants, one reaction rate constant k_f for the forward reaction and one reaction rate constant k_b for the backward reaction. These reaction rate constants are related via the equilibrium constant K via $K = k_f/k_b$. If the equilibrium constants K_i are specified for a multiequilibria system and one is interested in the determination of the concentrations of all species *at equilibrium*, then one can freely choose in each case either the forward or backward reaction rate constant and use the equation $K_i = k_{f,i}/k_{b,i}$ to determine the other. Hence, with the reaction free enthalpies ΔG_i reported here and some elemental knowledge of computing software (i.e., *Mathematica*, (60)), the fast and accurate computation of all equilibrium concentrations is feasible for any given set of initial conditions. On the other hand, if one is interested in the transient *kinetics of reaching the equilibrium*, then it no longer suffices to know only the ratios of the forward and backward reactions (i.e., the equilibrium constants) and one must also know one of the reaction rate constants for each elemental reaction (59). We are in the process of computing the activation barriers for the M^{2+} -catalyzed carbamylation reactions for simulations of the transient kinetics.

Electronic Structures and Spin Density Distributions of Formate Complexes of Open-Shell Systems

Molecular orbitals (MOs) with significant d-orbital involvement are shown in Figures 8 and 9, respectively, for iron formate, FeL_2 (d^6) and nickel formate, NiL_2 (d^8), respectively. The description of atomic orbital (AO) components of the MOs assumes that the molecules lie in the xy plane with the CH bonds aligned with the x-axis.

In the quasi spl-coordination, the lobes of the $d(xy)$ orbital are oriented toward the O atoms of the formate ligands and $d(xy)$ is the highest-lying d-orbital because of electron-electron repulsion. The lobes of the $d(yz)$ orbital are in the plane that is perpendicular to the molecular plane and mirrors the two ligands. The $d(xy)$ orbital is singly occupied in CuL_2 and it is left empty in NiL_2 , CoL_2 and FeL_2 . The $d(yz)$ orbital is doubly occupied in CuL_2 and NiL_2 , it is singly occupied in CoL_2 , and it is left empty in FeL_2 . The MO analysis helps to understand the spin density distributions of CoL_2 and CuL_2 (Figure 10).

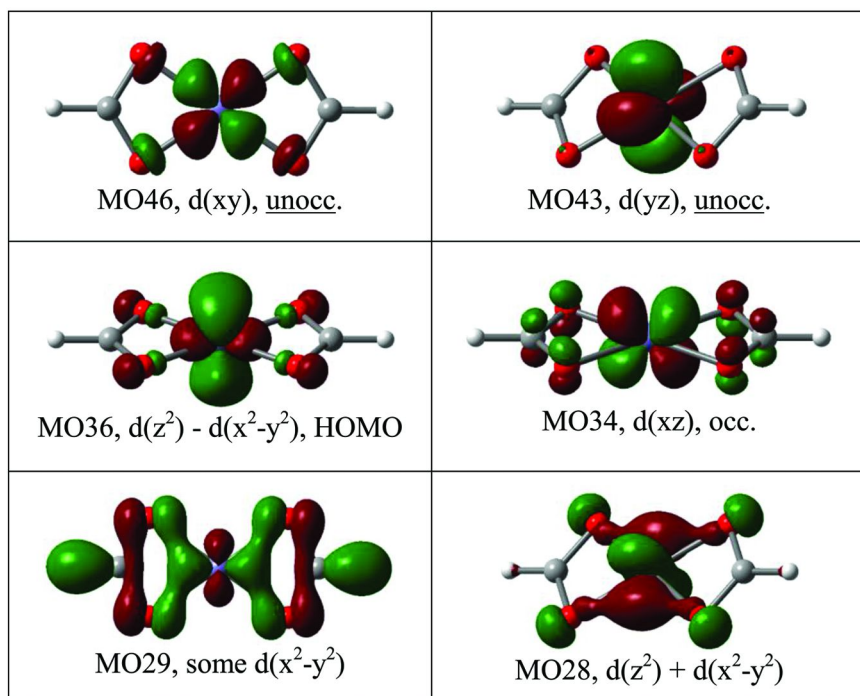


Figure 8. Selected MOs of iron formate, FeL_2 with significant d-orbital involvement. The description of AO components of the MOs assumes that the molecule lies in the xy plane with the CH bonds aligned with the x -axis.

For CoL_2 , one might expect single-occupation of the $d(z^2)$ MO because it is above the $d(yz)$ MO in NiL_2 . Nevertheless, CoL_2 features single-occupation of the $d(yz)$ orbital as is evidenced by the α -spin density in a $d(yz)$ -shaped region around the cobalt center. The α -spin density is largely localized at the Co-center with only minor spin polarization in the basins of the formate O atoms. Large α -spin density accumulation at the M^{2+} center might lead to spin-polarization of a coordinating CO_2 and influence its reactivity.

On the other hand, the spin density distribution of CuL_2 is more complex. The SOMO of CuL_2 involves the $d(xy)$ -MO as expected, but the excess α -spin density clearly is not localized in the $d(xy)$ -shaped region around the copper center. For CuL_2 , the MO analysis merely provides a starting point to think about the spin density and the actual spin density distribution shows large transfers of α -spin density from a $d(xy)$ -shaped region around copper toward the formate O-atoms.

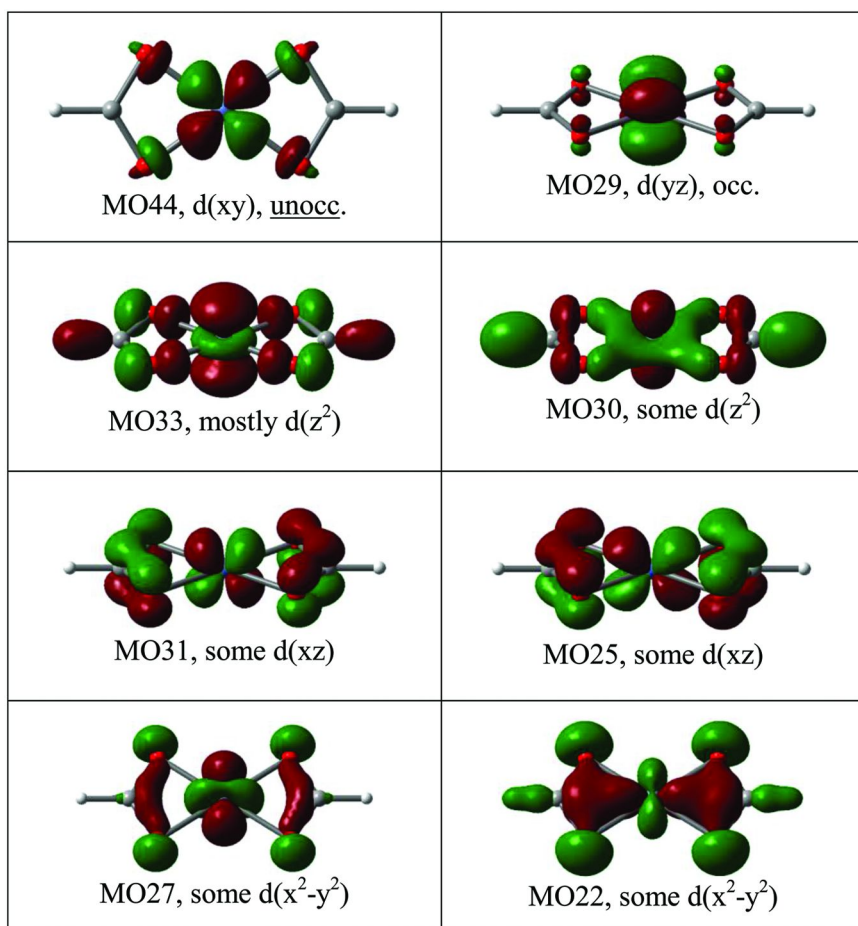


Figure 9. Selected MOs of nickel formate, NiL_2 with significant d -orbital involvement. The description of AO components of the MOs assumes that the molecule lies in the xy plane with the CH bonds aligned with the x -axis.

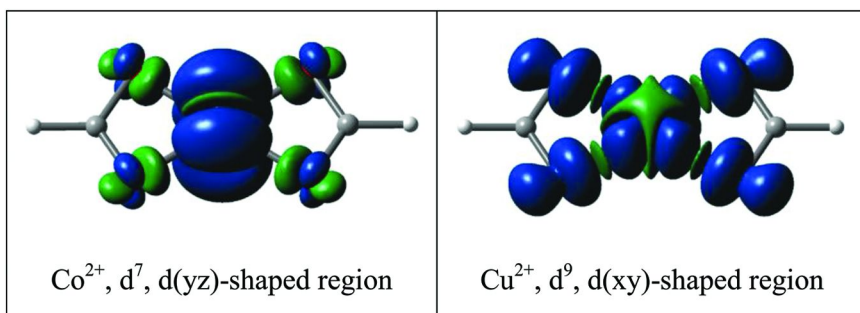


Figure 10. Spin density distributions of the formates CuL_2 and CoL_2 in their doublet states. The complete UMP2/6-31G* spin densities are shown for an isodensity value of 0.001 e/au^3 ; α -spin density is shown in dark grey (blue online) and β -spin density regions in light grey (green online). The description of d -type AO components assumes that the molecules lie in the xy plane with the CH bonds aligned with the x -axis.

Conclusions

The equilibrium $\text{CO}_2 + \text{H}_2\text{O}\cdot\text{ML}_2 \rightleftharpoons \text{OCO}\cdot\text{ML}_2 + \text{H}_2\text{O}$ lies very much on the left side: Water is great donor ligand, CO_2 is a comparatively poor donor ligand, and the $\text{H}_2\text{O}/\text{CO}_2$ exchange reaction is significantly endergonic for $\text{M}^{2+} = \text{Mg}^{2+}$ ($\Delta G_{\text{W}} = 15.2 \text{ kcal/mol}$). How can a reaction with such a large $\text{H}_2\text{O}/\text{CO}_2$ replacement penalty be nature's key to reversible CO_2 capture? Well, the "capture" reaction is only one side of the coin and the "release" reaction is just as important for "reversibility". Rubisco's $^{\text{A}}\text{CO}_2$ binding is reversible because of the large $\text{H}_2\text{O}/\text{CO}_2$ replacement penalty and this advantage of reversibility comes at the tolerable disadvantage of slow CO_2 loading. The equilibrium reaction $\text{CO}_2 + \text{H}_2\text{O}\cdot\text{ML}_2 \rightleftharpoons \text{OCO}\cdot\text{ML}_2 + \text{H}_2\text{O}$ may go back and forth many times, but an $\text{OCO}\cdot\text{ML}_2$ aggregate must eventually lead to CO_2 capture because only CO_2 can react with the lysine's amino group and because the carbamic acid complex $(\text{RNH})(\text{HO})\text{C}=\text{O}\cdot\text{ML}_2$ is bound much more strongly than CO_2 and also more strongly than H_2O . Water does not prevent CO_2 capture, it only slows it down, and more importantly, it is only for the sake of water that CO_2 release is feasible.

The enzyme rubisco employs magnesium and Mg^{2+} exhibits the highest $\text{H}_2\text{O}/\text{CO}_2$ replacement penalty among the metal ions studied here. The results show that the closed-shell systems Ca^{2+} and Zn^{2+} are excellent candidates for magnesium alternatives. The theoretical analysis further suggests that the open-shell transition metal ions Co^{2+} and Cu^{2+} also are interesting targets in the search for magnesium alternatives with similar size and comparable binding energies, and Co^{2+} is particularly interesting from a mechanistic perspective. The cobalt ion's spin density is localized at the Co^{2+} -center and may lead to spin-polarization of coordinating $\text{O}=\text{C}=\text{O}$ or $(\text{RNH})(\text{HO})\text{C}=\text{O}$ and influence their reactivities.

Acknowledgments

The author thanks the Chinese Academy of Sciences for the award of a Visiting Professorship for Senior International Scientists 2014 and Professor Wen-Hua Sun for being a most generous host. Part of the manuscript was written while the author was a Guest Professor in the College of Chemistry and Materials Science, Northwest University, Xi'an.

References

1. *First Successful Demonstration of Carbon Dioxide Air Capture Technology Achieved*; Earth Institute, Columbia University, April 25, 2007. physorg.com/news96732819.html (accessed February 27, 2015).
2. Keith, D. W.; Ha-Duong, M.; Stolaroff, J. K. Climate strategy with CO₂ capture from the air. *Clim. Change* **2006**, *74*, 17–45.
3. Socolow, R.; Desmond, M.; Aines, R.; Blackstock, J.; Bolland, O.; Kaarsberg, T.; Lewis, N.; Mazzotti, M.; Pfeffer, A.; Sawyer, K.; Siirola, J.; Smit, B.; Wilcox, J. *Direct Air Capture of CO₂ with Chemicals: A Technology Assessment for the APS Panel on Public Affairs*. American Physical Society, Washington, DC, June 1, 2011. <http://www.aps.org/policy/reports/assessments/upload/dac2011.pdf> (accessed February 27, 2015).
4. Zeman, F. S.; Lackner, K. S. Capturing carbon dioxide directly from the atmosphere. *World Resources Rev.* **2004**, *16*, 62–68.
5. Lackner, K. S.; Brennan, S. Envisioning carbon capture and storage: Expanded possibilities due to air capture, leakage insurance, and C-14 monitoring. *Clim. Change* **2009**, *96*, 357–378.
6. Sun, Z.; Fan, M.; Argyle, M. Supported monoethanolamine for CO₂ separation. *Ind. Eng. Chem. Res.* **2011**, *50*, 11343–11349.
7. Kuntz, J.; Aroonwilas, A. Performance of spray column for CO₂ capture application. *Ind. Eng. Chem. Res.* **2008**, *47*, 145–153.
8. Idem, R.; Wilson, M.; Tontiwachwuthikul, P.; Chakma, A.; Veawab, A.; Aroonwilas, A.; Gelowitz, D. Pilot plant studies of the CO₂ capture performance of aqueous MEA and mixed MEA/MDEA solvents at the University of Regina CO₂ capture technology development plant and the Boundary Dam CO₂ capture demonstration plant. *Ind. Eng. Chem. Res.* **2006**, *45*, 2414–2420.
9. Goepfert, A.; Czaun, M.; May, R. B.; Prakash, G. K. S.; Olah, G. A.; Narayanan, S. R. Carbon dioxide capture from the air using a polyamine based regenerable solid adsorbent. *J. Am. Chem. Soc.* **2011**, *133*, 20164–20167.
10. McDonald, T.; Lee, W. R.; Mason, J. A.; Wiers, B. M.; Hong, C. S.; Long, J. R. Capture of carbon dioxide from air and flue gas in the alkylamine-appended metal-organic framework mmen-Mg₂(dobpdc). *J. Am. Chem. Soc.* **2012**, *134*, 7056–7065.

11. Sumida, K.; Rogow, D. L.; Mason, J. A.; McDonald, T. M.; Bloch, E. D.; Herm, Z. R.; Bae, T.-H.; Long, J. R. Carbon dioxide capture in metal-organic frameworks. *Chem. Rev.* **2012**, *112*, 724–781.
12. Poloni, R.; Smit, B.; Neaton, J. B. Ligand-assisted enhancement of CO₂ capture in metal-organic frameworks. *J. Am. Chem. Soc.* **2012**, *134*, 6714–6719.
13. McDonald, T. M.; Mason, J. A.; Kong, X.; Bloch, E. D.; Gygi, D.; Dani, A.; Crocella, V.; Giordanino, F.; Odoh, S. O.; Drisdell, W. S.; Vlaisavljevich, B.; Dzubak, A. L.; Poloni, R.; Schnell, S. K.; Planas, N.; Lee, K.; Pascal, T.; Wan, L. F.; Prendergast, D.; Neaton, J. B.; Smit, B.; Kortricht, J. B.; Gagliardi, L.; Bordiga, S.; Reimer, J. A.; Long, J. R. Cooperative insertion of CO₂ in diamine-appended metal-organic frameworks. *Nature* **2015**, *519*, 303–319.
14. Yang, Z.-Z.; Song, Q.-W.; He, L.-N. *Capture and Utilization of Carbon Dioxide with Poly-Ethylene Glycol*, SpringerBriefs in Molecular Science; Springer: New York, 2012.
15. Li, L.; Fu, M.-L.; Zhao, Y.-H.; Zhu, Y.-T. Characterization of carbonic anhydrase II from *Chlorella vulgaris* in bio-CO₂ capture. *Environ. Sci. Pollut. Res.* **2012**, *19*, 4227–4232.
16. Glaser, R.; Castello-Blindt, P. O.; Yin, J. Biomimetic Approaches to Reversible CO₂ Capture from Air. *N-Methylcarbaminic Acid Formation in Rubisco-Inspired Models*. In *New and Future Developments in Catalysis. Activation of Carbon Dioxide*; Suib, S. L., Ed.; Elsevier Publishers: Amsterdam, The Netherlands, 2013; Chapter 17; pp 501–534.
17. Shively, J. M.; Van Keulen, G.; Meijer, W. G. Something about almost nothing: CO₂ fixation in chemautotrophs. *Ann. Rev. Microbiol.* **1998**, *52*, 191–230.
18. Kusian, B.; Bowien, B. Organization and regulation of cbb CO₂ assimilation genes in autotrophic bacter. *FEMS Microbiol. Rev.* **1997**, *21*, 135–155.
19. Hugler, M.; Sievert, S. M. Beyond the Calvin cycle: autotrophic carbon fixation in the ocean. *Ann. Rev. Marine Sci.* **2011**, *3*, 89–261.
20. Mueller-Cajar, O.; Badger, M. R. New roads lead to Rubisco in archaeobacterial. *BioEssays* **2007**, *29*, 722–724.
21. Taylor, T. C.; Andersson, I. Structure of a product complex of spinach ribulose-1,5-bisphosphate carboxylase/oxygenase. *Biochemistry* **1997**, *36*, 4041–4046PDB 1AUS.
22. Taylor, T. C.; Andersson, I. Structural transitions during activation and ligand binding in hexadecameric Rubisco inferred from the crystal structure of the activated unliganded spinach enzyme. *Nat. Struct. Biol.* **1996**, *3*, 95–101.
23. Gutteridge, S.; Newman, J.; Herrmann, C.; Rhoades, D. The crystal structures of Rubisco and opportunities for manipulating photosynthesis. *J. Exp. Botany* **1995**, *46*, 1261–1267.
24. Lundqvist, T.; Schneider, G. Crystal Structure of the ternary complex of ribulose-1,5-bisphosphate carboxylase, magnesium(II) and activator carbon dioxide at 2.3 Å resolution. *Biochemistry* **1991**, *30*, 904–908PDB 2RUS.
25. Mizohata, E.; Matsumura, H.; Okano, Y.; Kumei, M.; Takuma, H.; Onodera, J.; Kato, K.; Shibata, N.; Inoue, T.; Yokota, A.; Kai, Y. Crystal

- structure of activated ribulose-15-bisphosphate carboxylase/oxygenase from green alga *Chlamydomonas reinhardtii* complexed with 2-carboxyarabinitol-15-bisphosphate. *J. Mol. Biol.* **2002**, *316*, 679–691.
26. Baranowski, M.; Stec, B. Crystallization and characterization of *Galdieria sulphuraria* Rubisco in two crystal forms: structural phase transition observed in P21 crystal form. *Intl. J. Mol. Sci.* **2007**, *8*, 1039–1051.
 27. Hartman, F. C.; Harpel, M. R. Structure, function, regulation, and assembly of D-ribulose-1,5-bisphosphate carboxylase/oxygenase. *Annu. Rev. Biochem.* **1994**, *63*, 197–234.
 28. Cleland, W. W.; Andrews, T. J.; Gutteridge, S.; Hartman, F. C.; Lorimer, G. H. Mechanism of Rubisco: the carbamate as general base. *Chem. Rev.* **1998**, *98*, 549–561.
 29. Portis, A. R.; Li, C.; Wang, D.; Salvucci, M. E. Regulation of Rubisco activase and its interaction with Rubisco. *J. Exp. Botany* **2008**, *59*, 1597–1604.
 30. Tapia, O.; Fidder, H.; Safont, V. S.; Oliva, M.; Andrés, J. Enzyme catalysis: transition structures and quantum dynamical aspects: Modeling Rubisco's oxygenation and carboxylation mechanisms. *Int. J. Quant. Chem.* **2002**, *88*, 154–166.
 31. Oliva, M.; Safont, V. S.; Andres, J.; Tapia, O. Transition structures for D-Ribulose-1,5-bisphosphate carboxylase/oxygenase-catalyzed oxygenation chemistry: Role of carbamylated lysine in a model magnesium coordination sphere. *J. Phys. Chem. A* **2001**, *105*, 4726–4736.
 32. Glaser, R.; Wu, Z.; Lewis, M. A higher level ab initio quantum-mechanical study of the quadrupole moment tensor components of carbon dioxide. *J. Mol. Struct.* **2000**, *556*, 131–141.
 33. Glaser, R.; Lewis, M.; Wu, Z. Theoretical study of the quadrupolarity of carbodiimide. *J. Phys. Chem. A* **2002**, *106*, 7950–7957.
 34. Lewis, M.; Wu, Z.; Glaser, R. Polarizabilities of carbon dioxide and carbodiimide. Assessment of theoretical model dependencies on dipole polarizabilities and dipole polarizability anisotropies. *J. Phys. Chem. A* **2000**, *104*, 11355–11361.
 35. Lewis, M.; Glaser, R. Synergism of catalysis and reaction center rehybridization. A novel mode of catalysis in the hydrolysis of carbon dioxide. *J. Phys. Chem. A* **2003**, *107*, 6814–6818.
 36. Lewis, M.; Glaser, R. Synergism of catalysis and reaction center rehybridization. An ab initio study of the hydrolysis of the parent carbodiimide. *J. Am. Chem. Soc.* **1998**, *120*, 8541–8542.
 37. Lewis, M.; Glaser, R. Synergism of catalysis and reaction center rehybridization in nucleophilic additions to cumulenes: The one-, two- and three-water hydrolyses of carbodiimide and methyleneimine. *Chem. Eur. J.* **2002**, *8*, 1934–1944.
 38. This value was given erroneously as 12.3 kcal/mol in ref. 16; see discussion of Table 4 and footnote (h) of Table 4.
 39. Grimme, S. Density functional theory with London dispersion corrections. *WIREs Comput. Mol. Sci.* **2011**, *1*, 211–228.

40. Cremer, D. Møller-Plesset perturbation theory: from small molecule methods to methods for thousands of atoms. *WIREs Comput. Mol. Sci* **2011**, *1*, 509–530.
41. Møller, C.; Plesset, M. S. Note on an approximation treatment for many-electron systems. *Phys. Rev.* **1934**, *46*, 618–622.
42. Frisch, M. J.; Head-Gordon, M.; Pople, J. A. Semi-direct algorithms for the MP2 energy and gradient. *Chem. Phys. Lett.* **1990**, *166*, 281–289.
43. Head-Gordon, M.; Head-Gordon, T. Analytic MP2 frequencies without fifth order storage: Theory and application to bifurcated hydrogen bonds in the water hexamer. *Chem. Phys. Lett.* **1994**, *220*, 122–128.
44. Peng, C.; Ayala, P. Y.; Schlegel, H. B.; Frisch, M. J. Using redundant internal coordinates to optimize equilibrium geometries and transition states. *J. Comp. Chem.* **1996**, *17*, 49–56.
45. Tomasi, J.; Mennucci, B.; Cammi, R. Quantum mechanical continuum solvation models. *Chem. Rev.* **2005**, *105*, 2999–3093.
46. Da Silva, E. F.; Svendsena, H. F.; Merz, K. M. Explicitly representing the solvation shell in continuum solvent calculations. *J. Phys. Chem. A* **2009**, *113*, 6404–6409.
47. Francl, M. M.; Petro, W. J.; Hehre, Q. J.; Binkley, J. S.; Gordon, M. S.; DeFrees, D. J.; Pople, J. A. Self-consistent molecular orbital methods. 23. A polarization-type basis set for 2nd-row elements. *J. Chem. Phys.* **1982**, *77*, 3654–3665.
48. Rassolov, V. A.; Pople, J. A.; Ratner, M. A.; Windus, T. L. 6-31G* Basis set for atoms K through Zn. *J. Chem. Phys.* **1998**, *109*, 1223–1229.
49. Murray, C. W.; Verdonk, M. L. The consequences of translational and rotational entropy lost by small molecules on binding to proteins. *J. Comp.-Aided Mol. Des.* **2002**, *16*, 741–753.
50. Mammen, M.; Shakhnovich, E. I.; Deutch, J. M.; Whitesides, G. M. Estimating the entropic cost of self-assembly of multiparticle hydrogen-bonded aggregates based on the cyanuric acid-melamine lattice. *J. Org. Chem.* **1998**, *63*, 3821–3830.
51. Murphy, K. P.; Xie, D.; Thompson, K. S.; Amzel, L. M.; Freire, E. Entropy in biological binding processes: Estimation of translational entropy loss. *Proteins: Structure, Function, and Genetics* **1994**, *18*, 63–67.
52. Finkelstein, A. V.; Janin, J. The price of lost freedom: entropy of bimolecular complex formation. *Protein Eng.* **1989**, *3*, 1–3.
53. Wertz, D. H. Relationship between the gas-phase entropies of molecules and their entropies of solvation in water and 1-octanol. *J. Am. Chem. Soc.* **1980**, *102*, 5316–5322.
54. Frisch, M. J.; Trucks, G. W.; Schlegel, H. B.; Scuseria, G. E.; Robb, M. A.; Cheeseman, J. R.; Scalmani, G.; Barone, V.; Mennucci, B.; Petersson, G. A.; Nakatsuji, H.; Caricato, M.; Li, C.; Hratchian, H. P.; Izmaylov, A. F.; Bloino, J.; Zheng, G.; Sonnenberg, J. L.; Hada, M.; Ehara, M.; Toyota, K.; Fukuda, R.; Hasegawa, J.; Ishida, M.; Nakajima, T.; Honda, Y.; Kitao, O.; Nakai, H.; Vreven, T.; Montgomery, J. A., Jr.; Peralta, J. E.; Ogliaro, F.; Bearpark, M.; Heyd, J. J.; Brothers, E.; Kudin, K. N.; Staroverov, V. N.; Keith, T.; Kobayashi, R.; Normand, J.; Raghavachari, K.; Rendell, A.; Burant, J. C.;

Iyengar, S. S.; Tomasi, J.; Cossi, M.; Rega, N.; Millam, J. M.; Klene, M.; Knox, J. E.; Cross, J. B.; Bakken, V.; Adamo, C.; Jaramillo, J.; Gomperts, R.; Stratmann, R. E.; Yazyev, O.; Austin, A. J.; Cammi, R.; Pomelli, C.; Ochterski, J. W.; Martin, R. L.; Morokuma, K.; Zakrzewski, V. G.; Voth, G. A.; Salvador, P.; Dannenberg, J. J.; Dapprich, S.; Daniels, A. D.; Farkas, O.; Foresman, J. B.; Ortiz, J. V.; Cioslowski, J.; Fox, D. J. *Gaussian 09, Revision D.01*; Gaussian, Inc.: Wallingford, CT, 2013.

55. University of Missouri Bioinformatics Consortium. <http://umbc.rnet.missouri.edu> (accessed February 28, 2015).
56. Winter, M. *WebElements Periodic Table: The Periodic Table on the Web*. <http://www.webelements.com> (accessed February 28, 2015).
57. Glaser, R.; Horan, C.; Nelson, E.; Hall, M. K. Incipient nucleophilic attack as a probe for the electronic structure of diazonium ions. An analysis of neighboring group interactions in β -carboxyvinylidiazonium ions. *J. Org. Chem.* **1992**, *57*, 215–228.
58. Glaser, R.; Horan, C. J. Interpretation of neighboring group interactions in crystal structures. A solid state and quantum-chemical study of incipient nucleophilic attack in 2-diazonium benzoic acid and its benzoate. *Can. J. Chem.* **1996**, *74*, 1200–1214.
59. Glaser, R. E.; Delarosa, M. A.; Salau, A. O.; Chicone, C. Dynamical approach to multi-equilibria problems for mixtures of acids and their conjugated bases. *J. Chem. Educ.* **2014**, *91*, 1009–1016.
60. Mathematica. Wolfram Research. <http://www.wolfram.com/mathematica/> (accessed April 17, 2015).